JOURNAL OF AIRCRAFT
Vol. 46, No. 5, September–October 2009

Fatigue Life Estimation of Helicopter Landing Probe Based on Dynamic Simulation

Zheng Hong Zhu*
York University, Toronto, Ontario M3J 1P3, Canada
and
Michael LaRosa† and James Ma‡
Curtiss–Wright Flow Control Company, Mississauga, Ontario L5C 2V8, Canada

DOI: 10.2514/1.38345

This paper develops a framework of dynamic simulation driven fatigue life analysis of a landing probe system for a typical 12-ton tricycle landing gear helicopter for embarked operations on the typical frigate. By integrating a novel dynamic helicopter/ship interface simulation with the rainflow cycle counting method, fatigue spectra, including all possible probe load cases under the wide range of operating and environmental conditions, have been developed with a confidence level of greater than 99.9%: otherwise, they would be practically unobtainable, even by limited sea trial testing. Furthermore, the fatigue stresses of the probe assembly were obtained by the finite element method, and the cumulative fatigue damage analyses were conducted by monitoring the fatigue life of the critical locations on each component of the probe assembly using the Palmgren–Miner rule against the design life requirement. This new approach provides an innovative and efficient design tool, through virtual prototyping, that can speed up the design process and reduce cost.

Nomenclature

A	=	area of the oleo piston
$\overline{AB}$	=	distance from the trailing-arm/fuselage attachment point to the oleo attachment point
$\overline{AC}$	=	distance from the trailing-arm/fuselage attachment point to the axle attachment point
A_{eqx}	=	equivalent frontal area
A_{eqy}	=	equivalent side area
a_s	=	static load factor for radial probe loading
$b(q)$	=	oleo stroke-dependent damping coefficient
b_s	=	static load factor for the vertical probe loading
c_1	=	constant damping coefficient
c_2	=	viscous damping coefficient
c_3	=	hydraulic damping coefficient
D	=	damage contributions
D_t	=	total fatigue damage
d	=	tire diameter
F_D	=	oleo damping force
F_O	=	total oleo force
F_S	=	oleo spring force
F_T	=	vertical component of the tire force
F_{ext}	=	external force acting on the helicopter body
F_{max}	=	maximum static oleo friction force
F_r	=	radial probe load
F_t	=	tire force
F_v	=	vertical probe load
F_μ	=	oleo frictional force
K_c	=	corrosion factor
K_d	=	size effect factor
K_f	=	surface finish factor
K_l	=	impact load factor
K_r	=	reliability factor
K_t	=	temperature factor
k_{cable}	=	spring stiffness of the traversing cable
k_s	=	generic spring stiffness of the securing system
M_{ext}	=	external moment acting on the helicopter body
m	=	helicopter mass
m_s	=	mass of the securing system
m_w	=	unsprung wheel mass
N	=	number of cycles causing crack initiation
n	=	number of fatigue cycles
P	=	tire inflation pressure
P_r	=	rated tire inflation pressure
p_0	=	initial oleo gas pressure
q	=	displacement of suspension in the local coordinate system
S_e	=	corrected fatigue endurance stress limit
S_{e0}	=	nondegraded endurance stress limit
V_{rel}	=	body velocity relative to freestream wind
V_0	=	initial oleo gas volume
w	=	tire width
X	=	vector of translation displacement of the helicopter center of mass
x_s	=	displacement of the securing system
α	=	decay rate
γ	=	gas constant
δ	=	tire deflection
η_{cable}	=	viscous damping coefficient of the traversing cable
η_s	=	generic viscous damping coefficient of the securing system
μ	=	coefficient of friction
ρ	=	density of the air at sea level
σ	=	stress at critical locations
σ_a	=	alternating stress amplitude
σ_e	=	equivalent fatigue stress at zero mean stress
σ_m	=	mean stress
σ_y	=	material yield stress
τ	=	tire type

Received 1 May 2008; accepted for publication 14 February 2009.

*Assistant Professor, Earth and Space Science and Engineering Department, 4700 Keele Street. Lifetime Member AIAA.
†Mechanical Engineer, INDAL Technologies, Engineering Department, 3570 Hawkestone Road.
‡Manager of Structural Engineering, INDAL Technologies, Engineering Department, 3570 Hawkestone Road.

Subscripts

i	=	initial value of variable
x, y, z	=	x, y, z components

Superscripts

$\dot{}$	=	first time derivative
$\ddot{}$	=	second time derivative

I. Introduction

EMBARKED naval helicopters have a wide range of applications, from performing antisubmarine warfare and other combat missions from warships to search and rescue operations, such as medical evacuation of personnel from civilian vessels. To fulfill these diverse roles, shipboard helicopters must be operable in the greatest range of sea and wind conditions. Many systems have been developed to assist in the safe recovery and on-deck handling of embarked helicopters in severe sea and wind conditions. Among them, the recovery assist, secure and traverse (RAST) system[§] appeals most because it can safely recover, secure, and traverse shipboard helicopters without strictly requiring any personnel on the ship's flight deck. The RAST system provides the capability to secure a variety of helicopters (in terms of size and landing gear configuration) from ships in very high sea conditions, up to and including upper sea state 6.

The RAST system secures the helicopter onto the flight deck by engaging a helicopter-mounted probe, which is the only structural link between the helicopter and the ship's flight deck, as illustrated in Fig. 1. Depending on the sea conditions and operational factors, such as ship heading and ship speed relative to the principal sea direction, the probe will experience cyclic securing loads over a wide range of values that could lead to a sudden and catastrophic failure due to the accumulated fatigue damage to the probe structure. The failure of the probe may result in the loss of the helicopter and the lives of the personnel onboard; this is especially true in elevated sea conditions.

Traditionally, engineers and designers have relied on limited statistical data to estimate the probe's design load spectra and costly physical prototype tests to determine the fatigue life of the probe. Using this design process, it is difficult to fully evaluate the impact of the severe sea and wind conditions on the fatigue life of the probe because of the safety- and cost-prohibitive nature of sea trial testing. To overcome the limitation of the traditional design process, an innovative design framework has been developed that is capable of accurately analyzing the fatigue life of the probe assembly, as well as its individual components, in one single and integrated simulation environment in a time efficient manner. This framework of virtual prototyping includes nonlinear transient dynamic simulations of the helicopter/ship interface to develop fatigue load spectra, finite element (FE) analysis of the probe assembly, and the cumulative fatigue damage analysis. The successful implementation of this novel solution allows for the prediction of the fatigue life of the probe without physical fatigue prototype tests.

II. Description of the Helicopter Landing Probe Assembly

The primary airborne structural element of the helicopter-securing system is the three-stage telescopic cylindrical retractable probe. It consists of three primary structural components: the shaft, the inner housing, and the outer housing, as shown by the solid model of Fig. 2. The shaft and inner housing are fully retracted into the outer housing when not required in the normal flight condition, and they are fully extended by an embedded spring, activated by the pilot in the cockpit, for capture during the landing, traversing, launching, and other on-deck operations. After being secured by the shipborne RAST rapid securing device (RSD), the probe shaft reacts the dynamic securing loads due to ship motion and wind environment. The principle

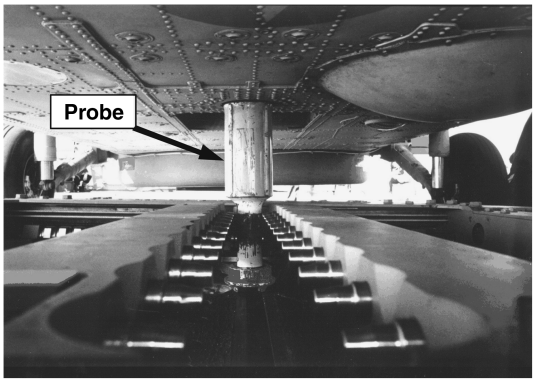

Fig. 1 RAST probe being secured in a RSD.

structural elements (PSEs) in the probe assembly are the shaft, the inner and outer housings, the crenellated ring, and the spherical nut. It should be noted that when the probe is secured by the RSD, the horizontal loading is continuously reacted by the probe. However, the probe can only react the downward vertical loads to restrain the helicopter from moving upward, relative to the ship deck under severe ship motion conditions, when the crenellated ring is in contact with the bottom of the RSD arresting beams.

The structural integrity and strength of the probe assembly was analyzed using the FE method. The interactions among the probe components and the helicopter structure are complicated and unknown in advance. A contact solution algorithm [1] was adopted for the analysis of the probe assembly to solve for the interactions and stresses simultaneously in order to eliminate the error sources in estimating the interaction forces. The contact solution algorithm transfers the loads from the shaft tip to the helicopter structure automatically, according to the geometry and stiffness of each contacting part, and then solves for the contact region and associated stresses. These local contact stresses were used in the optimization of the local contact areas as well as the geometry size and shape of each component.

III. Modeling of Helicopter/Ship Dynamic Interface

Traditional approaches to the helicopter/ship dynamic interface use static, quasi-static, and frequency-domain analyses [2] to estimate the securing requirements of helicopters on small ships and neglect important factors influencing the helicopter/ship interface dynamics. During various onboard operations, a helicopter may experience securing loads generated by geometrically nonlinear and time-dependent ship motion, deck reaction forces through the helicopter suspensions (such as nonlinear and intermittent tire contact and sliding), time- and displacement-dependent helicopter rotor forces and moments, and aerodynamic forces. The time dependence and the nonlinearity nature of the problem require a thorough and robust nonlinear analysis of the coupled equations of motion to describe the characteristics of the helicopter/ship interface and the forces acting on the helicopter. Figure 3 shows a 16-degree-of-freedom (DOF) helicopter/ship interface model, including three translations and three rotations for the ship, three translations and three rotations for the helicopter body, one prismatic or revolute DOF per suspension (three in total), depending on the suspension type, and one-DOF for the RSD in the ship's longitudinal axis. The main driving force in the helicopter/ship dynamic interface model is the time-varying ship motion that has been calculated using response amplitude operator spectra defined in the frequency domain [3]. However, it should be noted that the spectrum approach for the ship motion is a linear analysis and is applicable up to a significant wave height (SWH) of 6 m (upper sea state 6) [4]. The 16-DOF helicopter/ship interface model in Fig. 3 has been developed and implemented into aircraft/ship dynamic interface analysis simulation program Dynaface [5–7] by Curtiss–Wright Controls Engineered Systems-Marine Defense and will be used to determine the dynamic helicopter/ship interface loads.

[§]Data available online at http://www.indaltech.com/products/spokes/01a_RAST.htm [retrieved 17 July 2009].

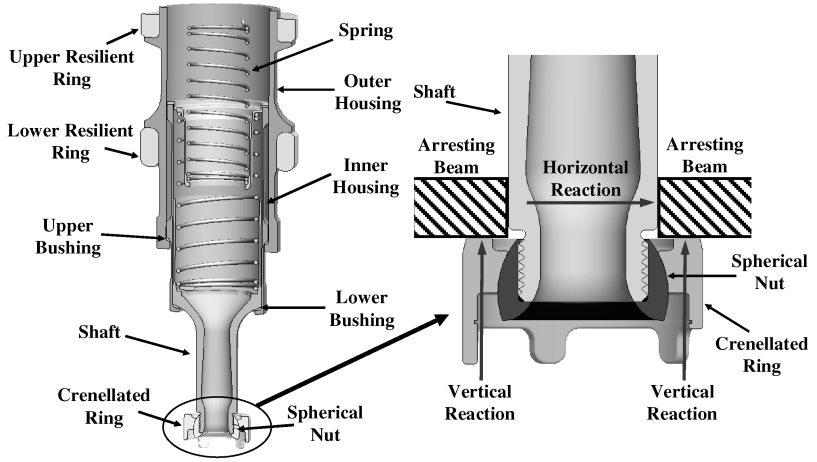

Fig. 2 Structural configuration of probe assembly.

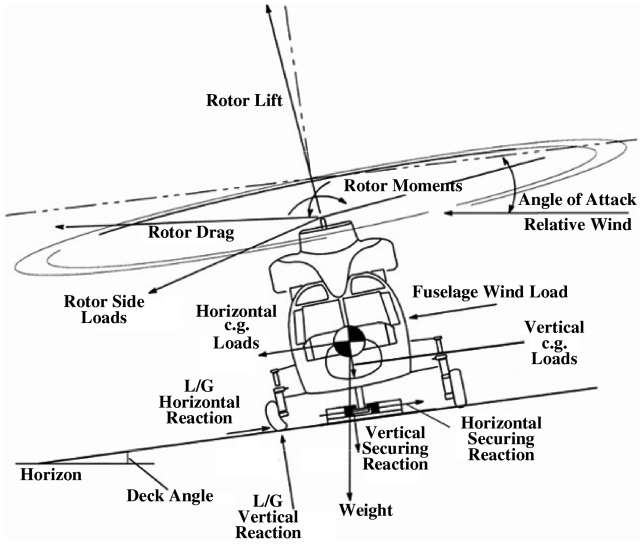

Fig. 3 Schematic of helicopter/ship interface model. (L/G represents landing gear.)

A. Equations of Motion of Helicopter

Consider the helicopter model shown in Fig. 3. A system of Cartesian coordinates $Oxyz$ is selected to describe the motion of the helicopter with its origin located at the c.g. of the helicopter in which x, y, and z denote the forward, lateral, and upward directions of the helicopter, respectively. The equations of motion of the helicopter can be expressed in terms of force and moment equilibrium in the helicopter frame as

$$m\ddot{\boldsymbol{X}} = \sum \boldsymbol{F}_{\text{ext}} \tag{1}$$

$$\mathrm{I}\,\dot{\boldsymbol{\Omega}} + \boldsymbol{\Omega} \times \mathrm{I}\boldsymbol{\Omega} = \sum \boldsymbol{M}_{\text{ext}} \tag{2}$$

where m and I are the mass and moment of inertia matrix of the helicopter about its c.g., $\boldsymbol{X}$ is the vector of translational displacement of the helicopter's c.g. in an inertial system, and $\boldsymbol{\Omega}$ is the angular velocity of the helicopter described in the helicopter frame. The external force $\boldsymbol{F}_{\text{ext}}$ and moment $\boldsymbol{M}_{\text{ext}}$ will be determined in the following sections.

B. Equation of Suspension Systems

There are two widely used suspension configurations implemented in the model: 1) the cantilever (or vertical oleo) and 2) the leading/trailing-arm suspensions, as shown schematically in Fig. 4. The cantilever-type suspension requires a translational DOF, whereas the trailing-arm suspension requires an angular DOF. Both of these suspension types have been simplified as a mass-spring-damper system. Considering the fact that the mass of the helicopter body is several orders higher than the suspensions, the helicopter body and suspensions can be decoupled dynamically to improve the computational efficiency without sacrificing accuracy.

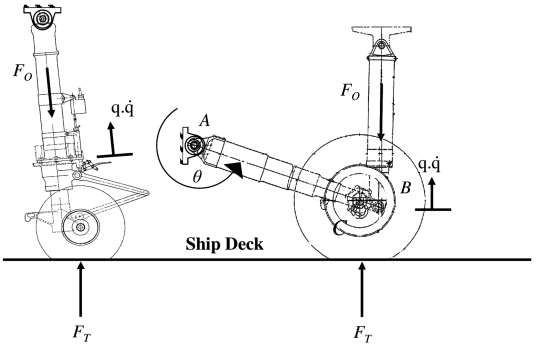

Fig. 4 Schematic representation of helicopter suspensions: a) cantilever and b) trailing-arm suspension.

In general, the dynamic equation of the suspension can be expressed as

$$m_w \ddot{q} = \begin{cases} F_T - F_O & \text{cantilever suspension} \\ \frac{\overline{AC}}{\overline{AB}} F_T - F_O & \text{trailing-arm suspension} \end{cases} \tag{3}$$

where F_T is the vertical component of the tire force, m_w is the effective mass associated with the suspension (depending on the suspension configuration), $\ddot{q}$ is the acceleration of the suspension in the local coordinate system, and F_O is the oleo force consisting of a spring-damper system with friction contributions, such that

$$F_O = F_S + F_D + F_\mu \tag{4}$$

where F_S, F_D, and F_μ are the spring, damping, and frictional forces of the gas oleo in response to the relative displacements and velocities, respectively.

1. *Oleo Spring Force*

The oleo spring force results from compressing a volume of gas enclosed within the oleo. Figure 5 illustrates the model used to evaluate the oleo spring force. The first region (region 1) represents the unusual case of oleo extension and is modeled by a linear spring. Oleo compression in region 3 is modeled using the ideal gas law for the primary compression region, such that

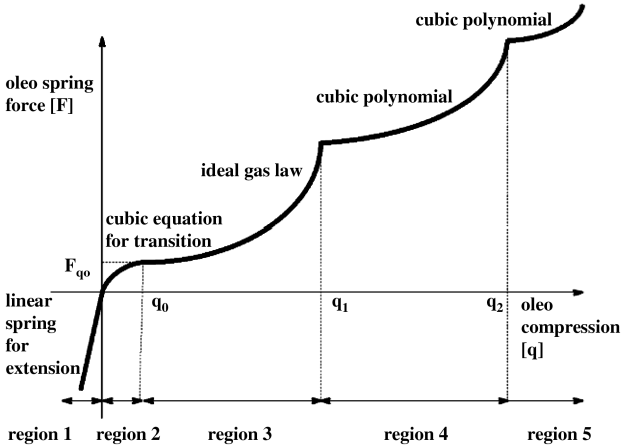

Fig. 5 Schematic representation of a typical oleo spring model.

$$F_S = \frac{p_0 V_0^{\gamma} A}{(V_0 - Aq)^{\gamma}} \tag{5}$$

where p_0 and V_0 are the initial gas pressure and volume with the oleo fully extended, γ is the gas constant, A is the area of the oleo piston, and q is the oleo compression displacement. To guarantee a continuous and differentiable transition between regions 1 and 3, region 2 is described using a cubic polynomial, though the extent of the transition region has been exaggerated for clarity in Fig. 5. Oleos containing multiple stages beyond region 3 are modeled using third-order polynomials.

2. Oleo Damping Force

Damping in the oleo may consist of constant, viscous, or hydraulic damping effects, individually or in combination. As a result, a generic damping force model is given as

$$F_D = c_1 + c_2\dot{q} + c_3\dot{q}^2 \tag{6}$$

where $\dot{q}$ is the velocity of the stroke and c_1, c_2, and c_3 are the damping coefficients for the constant, viscous, and hydraulic damping. If pressure relief valves are included, a multistage damping model can be used, as shown in Fig. 6. For the case of an oleo containing a metering pin that continuously varies the orifice size, the constant and viscous damping effects can be neglected, and the resulting force is dependent on both oleo stroke and velocity, such that

$$F_D = \sum_{i=0}^{n} b_i(q)\dot{q}^2 \tag{7}$$

where $b_i(q)$ are the stroke-dependent damping coefficients.

3. Oleo Friction Force

Finally, the oleo friction force is defined as [8]

$$F_{\mu} = (\dot{q}/|\dot{q}|)F_{\max}[1 - \exp(-\alpha|\dot{q}|)] \tag{8}$$

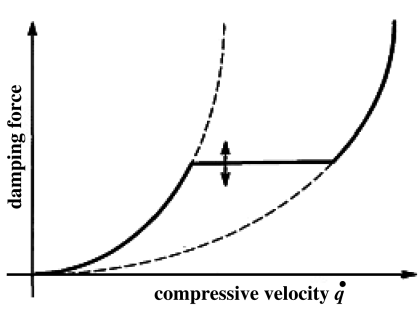

Fig. 6 Typical damping characteristic for a gas oleo, including the effect of a pressure relief valve.

where α is the decay rate of the modified friction model, q is the suspension configuration coordinate, and $F_{\max}$ is the maximum static oleo friction force.

C. Equations of Tire Model

The tires are one of the most important elements in the helicopter/ship interface system, as they form the primary interface between the helicopter and the ship. Tire forces are calculated using the tire model of Smiley and Horne [9], such that

$$F_{tx} = [0.53d(P + 4P_r)\sqrt[3]{\delta_z/d}]\delta_x \tag{9}$$

$$F_{ty} = [\tau w(P + 0.24P_r)(1 - 0.7\delta_z/w)]\delta_y \tag{10}$$

$$F_{tz} = f(\tau, w, d, P, P_r, \delta_z) \tag{11}$$

where F_{tx}, F_{ty}, and F_{tz} are the components of tire force in the longitudinal, lateral, and vertical directions; P is the inflation pressure; P_r is the rated pressure; τ is the tire type; d is the tire diameter; w is the tire width; δ_x, δ_y, and δ_z are the longitudinal, lateral, and vertical tire deflections; and f is the vertical tire force function obtained from experiments.

The preceding tire model is highly nonlinear because the instantaneous tire inflation pressure is dependant on the tire deflection and its rate. The exact values of the tire forces are determined by an iterative process using previous state parameters as input to the tire model, such as the vertical tire deflection, local tire velocity, lateral and longitudinal distances the wheel hub has traveled, the previous lateral tire deflection, the contact condition with the ship deck, etc. Detailed expressions can be found in [9].

D. Aerodynamic Effects

Aerodynamic forces acting on the helicopter result from the fuselage drag and the rotor-induced forces and moments. Aerodynamic drag is calculated based on the equivalent frontal and side areas of the helicopter fuselage and the relative wind speed, such that

$$F_{D_{x,y}} = \tfrac{1}{2}\rho V_{\mathrm{rel}_{x,y}}|V_{\mathrm{rel}_{x,y}}|A_{\mathrm{eq}_{x,y}} \tag{12}$$

where $A_{\mathrm{eq}_{x,y}}$ are the equivalent frontal and side areas, respectively; taking into account the coefficient of drag, ρ is the density of air at sea level, and $V_{\mathrm{rel}_{x,y}}$ are the body velocities relative to the freestream wind in the longitudinal and lateral directions, respectively.

The rotor thrust is modeled using a constant thrust value during the descent phase of the touchdown transient, followed by decaying rotor thrust as the pilot reduces the rotor collective to its minimum. This optional decreasing thrust can be triggered by the first wheel contact with the deck. In addition, an embarked helicopter, even with the rotor at its minimum collective, will experience additional rotor lift due to the angle of attack of the rotor disc relative to the apparent wind, as a result of angular ship motions, as shown in Fig. 7. Wind-tunnel experiments [10,11] have demonstrated that the wind-induced rotor thrust can be as high as 25% of the helicopter weight for the case in which the rotor collective is at its minimum. Consequently, potentially large rotor forces and moments can be developed. These effects are evaluated continuously throughout the simulation, based on aircraft manufacturer rotor data at different instantaneous wind conditions and angle of attack.

E. Securing System

The securing system consists of the airborne probe assembly and the shipborne RSD assembly. The securing system is simplified as a generic spring-damper system and a single-DOF lumped mass-spring model linking the helicopter and the ship deck such that

$$m_s\ddot{x}_s + (\eta_{sx} + \eta_{\mathrm{cable}})\dot{x}_s + (k_{sx} + k_{\mathrm{cable}})x_s = 0 \tag{13}$$

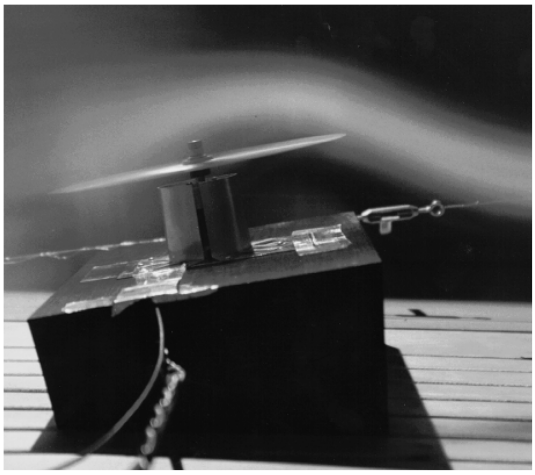

Fig. 7 Visualization of airflow over a typical frigate flight deck.

$$F_{y,x} = k_{\bar{s}y,z}\delta_{s_{y,z}} + \eta_{\bar{s}y,z}\dot{\delta}_{s_{y,z}} \tag{14}$$

where $k_{sx,y,z}$ and $\eta_{sx,y,z}$ are the spring stiffness and viscous damping coefficients of the generic spring model in x, y, and z directions, and k_{cable} and η_{cable} are the spring stiffness and viscous damping coefficients of the traversing cable connecting the RSD, respectively.

The stiffness of the generic spring in each of the three principal directions are evaluated by considering the flexibility of the helicopter fuselage, the probe assembly, the RSD, and the ship deck in series in three principal directions. The spring is assumed to connect the helicopter to the ship directly in the ship's vertical and lateral directions. In the longitudinal direction, the spring connects to the lumped mass of the RSD and then the ship, via the traversing cable.

IV. Critical Locations and Load Factors in Probe Components

The fatigue life of the probe assembly is dictated by the crack initiation at the critical locations of each component. These critical locations can be identified through a static strength analysis for the solid model of the probe assembly by applying the design vertical and radial probe loads separately, using the FE method. By applying the vertical and radial probe loads separately, the static analyses can determine 1) the radial and vertical stiffness of the probe assembly for the dynamic helicopter/ship interface simulation, 2) the critical high-stressed locations in the probe assembly, and 3) the load factors relating the critical high stress to the probe loads. Figures 8–11 show areas of high stress in the PSEs: the shaft, the inner housing, the outer housing, and the spherical nut and crenellated ring of a typical probe

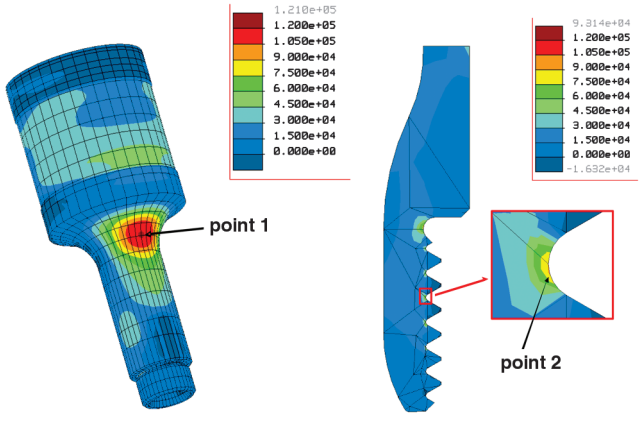

Fig. 8 Critical locations on the probe shaft: a) radial load only and b) vertical load only.

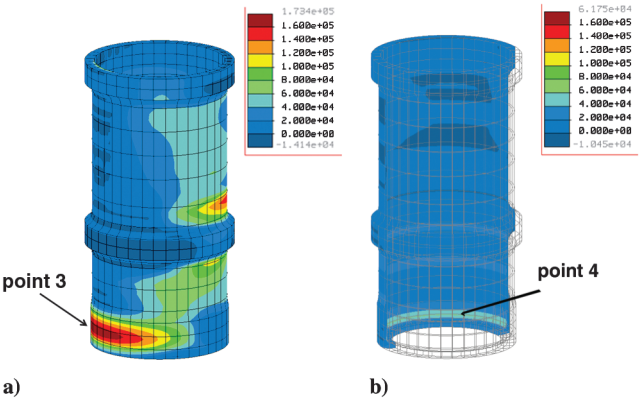

Fig. 9 Critical locations on the inner housing: a) radial load only and b) vertical load only.

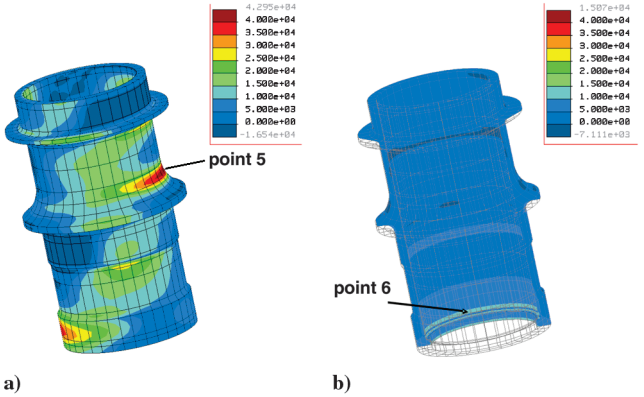

Fig. 10 Critical locations on outer housing: a) radial load only and b) vertical load only.

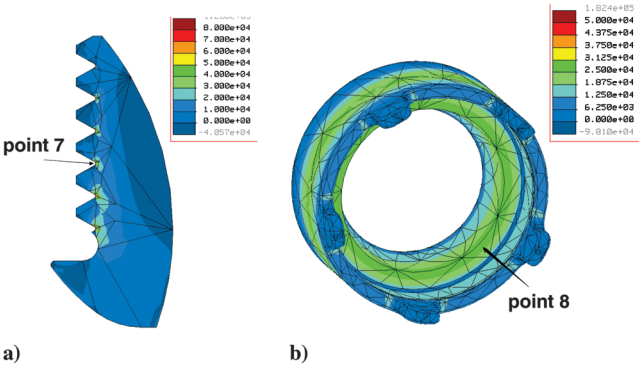

Fig. 11 Critical location on the a) spherical nut and b) crenellated ring.

assembly, respectively. Recall that the spherical nut and the crenellated ring react the vertical loads only as the radial loads are applied above the crenellated ring (refer to Fig. 2).

The most critical points in each probe component are summarized in Fig. 12. Each point was selected as being the most critical based on the applied loading direction. For example, two points on the shaft have been identified. Point 1 is the peak stress as a result of radial loading only, and point 2 is the peak stress as a result of vertical loading only. The same approach was used for the inner and outer housing, in which the peak stresses identified by points 3 and 5 are the results of radial loading, and points 4 and 6 are the results of vertical loading. Recall that the spherical nut and crenellated ring experience vertical loading only. Therefore, points 7 and 8 highlight the peak stresses in the spherical nut and crenellated ring, respectively, resulting from vertical loading.

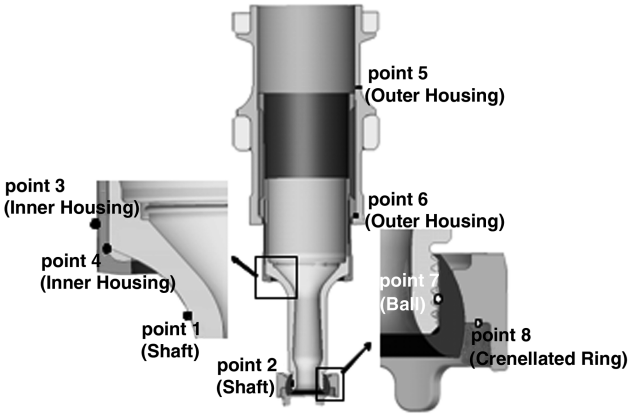

Fig. 12 Critical locations in probe components for fatigue analysis.

Having identified the critical locations, a relationship between each probe load component and the resulting stresses at each critical point is established, such that

$$\sigma = a_s F_r + b_s F_v \tag{15}$$

where F_r and F_v are the unit radial and vertical probe load components, a_s and b_s are the associated load factors, and σ is the stress at the critical locations. The load factors a_s and b_s are determined by measuring the stress values at the critical points subject to the unit radial and vertical probe load separately. Thus, the dynamic stresses $\sigma(t)$ at the critical locations can be obtained by substituting the time histories of radial $F_r(t)$ and vertical $F_v(t)$ load components into Eq. (15).

V. Fatigue Load Spectra Parameters

To predict the likely probe life, in terms of fatigue, a suitable description of the fatigue load spectra that the helicopter probe can be expected to experience throughout its life when embarked on a frigate-sized vessel is required. Dynamic helicopter/ship interface simulations, using Dynaface, will generate an appropriate probe securing load spectrum to be used in the fatigue life estimation. Therefore, several parameters pertinent to the dynamic helicopter/ship interface must be carefully identified in the simulations in order to develop a realistic load spectrum. These include 1) sea state conditions (i.e., SWH, wave modal period, wind speed and direction, and sea state probabilities to be considered to formulate the design spectrum); 2) ship operations (i.e., ship speed, ship heading, and probability of operation); 3) helicopter configuration and on-deck configurations; and 4) helicopter launch and recovery time periods.

A. Sea State Conditions

The typical objectives of a government defense policy include homeland security, defense of continent, and contribution to international security. As a result, ships can be placed in a variety of sea regions around the world. Because the most severe sea conditions can typically be found in the North Atlantic Ocean, the analyses considered sea conditions associated with both the open ocean and littoral waters of the North Atlantic Ocean. The distribution of sea states is summarized in Fig. 13a for the open ocean, based on information provided in the NATO Standardized Agreement 4194 [12]. Considering the fact that an embarked helicopter will not operate on deck beyond sea state 6, the sea state probabilities shown in Fig. 13a were normalized to exclude sea states greater than 6 as summarized in Fig. 13b.

To define the sea conditions associated with a particular sea state, a description of the SWH, modal period, and wind speed must be provided. Table 1 summarizes the SWH, modal period, and sustained wind speed for each sea state used in the simulation [13]. The SWH represents the upper bounds of the sea state, the modal period represents the most probable value for the sea state, and the wind

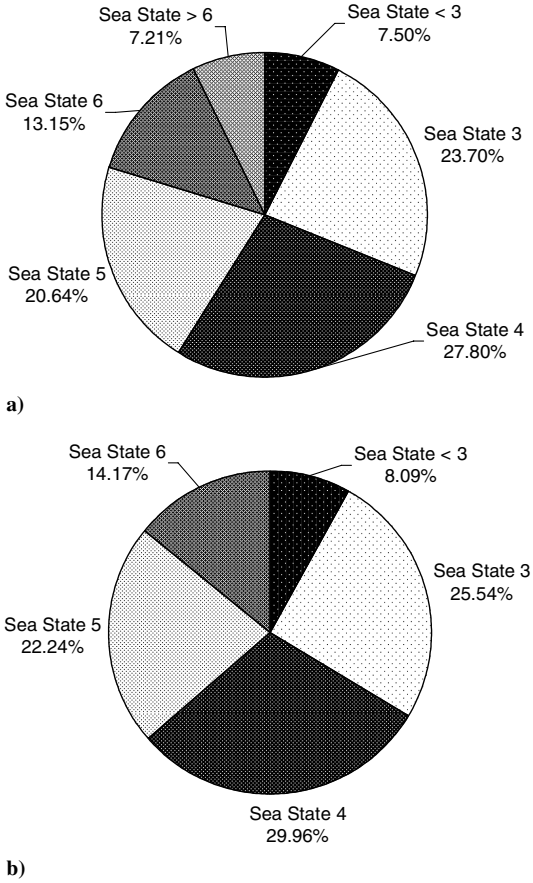

Fig. 13 Distribution of sea state for the North Atlantic Ocean: a) all sea states and b) normalized distribution excluding sea states above sea state 6.

speeds are applicable at a height of 10 m above sea level, as a helicopter on a typical frigate is located approximately at this height.

From dynamic interface analyses, it was found that probe loads occurring in sea states less than 3 were low and would not significantly affect the fatigue life. Thus, the dynamic helicopter/ship interface analyses were carried out only for sea states 3–6 in order to generate the fatigue load spectrum. In addition, all operational cases were analyzed with the wind direction aligned with the principal sea direction, as is the case for developing seas. However, in sea states 5 and 6, wind directions of ± 30 deg relative to the principal sea direction were also considered to account for instances in which the wind is not aligned with the direction of the sea. These were assumed to apply 25% of the time in each direction. The wind was assumed aligned with the sea direction for the remaining 50% of the time. The actual apparent wind speed and direction over the flight deck is calculated as the resultant of the wind vectors arising from the true wind speed and the ship speed.

B. Ship Operation

The ship's response to the seaway was assumed symmetrical about its longitudinal axis, as is usually the case with linear ship motion analysis. Consequently, the value at a heading of 60°, for example,

Table 1 Normalized North Atlantic sea conditions for fatigue analysis [13]

Sea state number	SWH, m	Modal period, s	Wind speed, m/s, (kt)
<3	0	7.5	0
3	1.25	8.8	5.6 (11)
4	2.5	9.7	8.2 (16)
5	4.0	10.9	10.7 (21)
6	6.0	11.5	13.8 (27)

will be the same as that at 300°. It is possible, therefore, to choose ship headings from the range 0 to 180° where 0° corresponds to head seas, 90° corresponds to starboard beam seas, and 180° corresponds to following seas. Although only half of the headings were used in dynamic simulations for the fatigue analysis (0–180°), the statistics for 0 through 360° were considered. The ship is assumed to spend equal time at all headings relative to the principal sea direction in 15° increments. This assumption is conservative regarding the fatigue life estimation as, in reality, the ship will likely be in more favorable headings for a larger portion of the time.

Ship speeds for a typical frigate range from 0 to 15.4 m/s (0–30 kt) [14]. However, the ship's likely speed is dictated by the mission, with the economical cruising speed frequently used. Very high and very low speeds are rare. Typical frigates have an economical cruising speed of 7.7 m/s (15 kt) [15]. Figure 14a shows the probability distribution of ship speed for a typical warship, used for the purpose of this fatigue analysis [14,16,17]. Note that in rough seas it becomes increasingly difficult to obtain high speeds, due to increased ship motion, slamming, and deck wetness. Therefore, for the purpose of the fatigue analysis, the ship speed of 15.4 m/s (30 kt) will not be included for sea state 6 only. As a result, the probability distribution of ship speeds was renormalized for sea state 6, as shown in Fig. 14b.

C. Helicopter Configuration

1. Embarked Operation Cycles

Typical maritime helicopters have a minimum useful life of 10,000 flight hours. Because embarked helicopters are not necessarily assigned to an individual ship for the entire life of the helicopter, and ships are typically at sea for 20–40% of the time, it can be expected that an embarked helicopter will conduct both shore-based and embarked operations throughout the course of its life. A typical usage rate as a percentage of the annual flying rate can be approximately 55% shore-based and 45% embarked. Therefore, approximately 4500 flights hours out of the minimum useful life of 10,000 flight hours can be considered as embarked operations. Considering that helicopter manufacturers typically assume 1.5 cycles (1 cycle = 1 takeoff and 1 landing evolution) of probe operation per embarked flight hour, [18] it is reasonable to assume the minimum number of embarked cycles over the useful life of the helicopter is approximately $1.5 \times 4500 = 6750$ cycles. Furthermore, the average annual flying rate is dictated by the type of missions expected from the helicopter and available funding. However, for maritime helicopters, approximately 400 flight hours per year can be expected for a useful life of 25 years. Therefore, a typical probe will experience approximately 270 cycles of embarked operation per year.

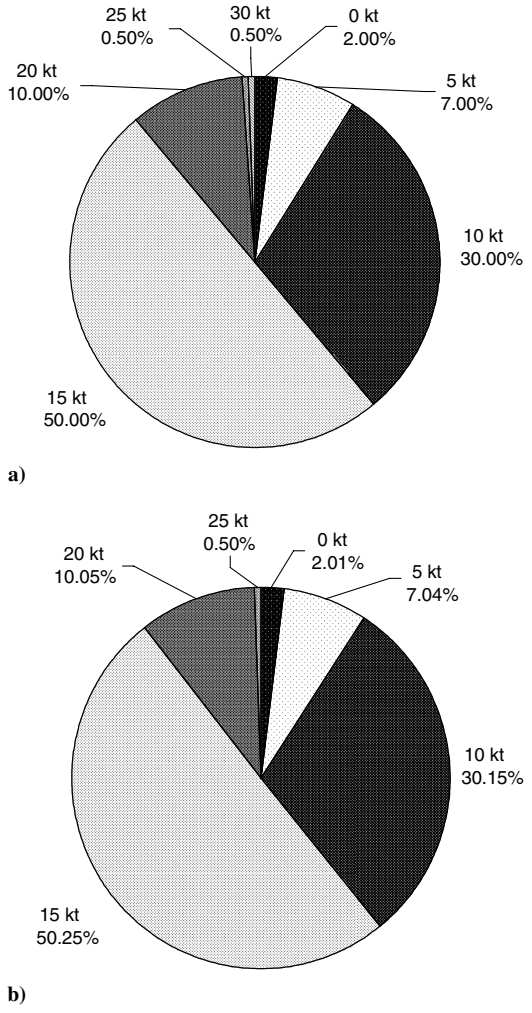

Fig. 14 Distribution of ship speed a) for sea states 3–5 and b) for normalized ship speed excluding 30 kt for sea state 6.

2. Weight of Embarked Helicopter

Most embarked helicopter sortie profiles typically involve the helicopter taking off at its maximum gross weight. However, upon return from a mission, the helicopter may not necessarily be at its minimum landing weight. In addition, to ensure a constant state of readiness, maritime helicopters are typically refueled before being traversed into the hangar. Therefore, for this analysis, the helicopter is assumed to be at the maximum weight 75% of the time and minimum landing weight 25% of the time.

3. Alignment of Embarked Helicopter with Ship Centerline

The RAST system is capable of securing a helicopter with a misalignment of up to ±30 deg yaw from the ship's centerline. However, experienced pilots are rarely misaligned with the ship's centerline by more than ±5 deg upon touchdown, even under extreme conditions. Therefore, sea states 5 and 6 were analyzed both with the helicopter aligned and misaligned, having an assumed distribution of 80% at 0 deg alignment and 10% each for +30 and −30 deg alignment. These probabilities occur for the recovery and straightening phases of embarked operations. For all other on-deck operations (i.e., traverse and launch), the helicopter is always aligned with the ship's centerline. For sea states less than 5, the helicopter is assumed aligned because it will be for the majority of the time.

In the event that the helicopter lands misaligned with the track centerline, the next step would be to straighten the helicopter. As most naval helicopters have a free-swiveling auxiliary gear, numerous gear angles are possible. It is ultimately up to the system operator as to the sequence of maneuvers that will be required to straighten the helicopter. Therefore, it was assumed in this analysis that the helicopter will spend 50% of the straightening time with the auxiliary gear aligned (0 deg) and 50% at 90 deg for a given straightening evolution.

D. Launch and Recovery Time Assessment

The typical operating cycle times are summarized in Table 2, based on data contained in MIL-SPEC MIL-R-85111A [19]. Table 3 expands the description to include assumed estimates of the time spent with various combinations of landing gear brake status (disengaged and engaged) and rotor status (stopped and turning). Although not strictly required when using the RAST system, typical

Table 2 RAST operating cycle times

	Time, min
Traverse to designated landing area (DLA)	5
Launch	15
Recovery	15
Straightening and traverse to hangar	10
Total	45

Table 3 Rotor and brake status for RAST operation

	Time, min	Brakes status	Rotor status
Traverse (hangar to DLA)	5.0	Off	Stopped
Launch–secured	12.5	On	Stopped
Launch–secured	2.5	On	Turning
Recovery–secured	2.5	On	Turning
Recovery–secured	12.5	On	Stopped
Straighten and traverse to hangar	10.0	Off	Stopped

embarked helicopter operating procedures stipulate that the helicopter is to be lashed before launch and following recovery. However, it was conservatively assumed that lashings were not applied. It should be noted that helicopters fitted with a probe perform both free-deck (i.e., helicopter lands with the probe within the capture area of the RSD but is not secured by the RSD) and captured landings. Free-deck landings are typically performed in lower sea states, as the ship motions are less severe. However, for the fatigue analysis, it was conservatively assumed that the probe is always secured by the RSD when the helicopter is on deck. It was also assumed that the helicopter is lashed at all times that it is not involved in a flight cycle.

VI. Fatigue Life Analysis and Results

A. Fatigue Stress Spectra

The combination of the probabilities of operating conditions and the knowledge of helicopter operating procedures summarized in the previous sections resulted in approximately 12,000 simulation cases. Each case was run for 30,000 s in order to ensure that typical fatigue loading of the probe would be captured and used for subsequent analysis. The fatigue stress at each critical point was calculated by converting the probe load time histories from the dynamic helicopter/ship interface simulations using Eq. (6). The fatigue stress spectrum at each critical point was then generated by processing the fatigue stress time histories using a rainflow cycle counting method, as described in the American Society for Testing and Materials Standard E1049-85 [20], for each operating condition by enumerating the number of fatigue cycles associated with all combinations of stress ranges and their mean value. Based on the knowledge of the amount of time the probe is expected to experience for each of the operating conditions, the corresponding rainflow chart developed was weighted by an appropriate probability of occurrence for that condition. The cumulative rainflow matrices corresponding to each of the orthogonal securing load directions were converted from the expected number of stress cycles per year to the total number of stress cycles expected over the design life of the probe. This provides a summary rainflow chart that is the weighted sum of the rainflow charts corresponding to each simulation case. Figures 15 and 16 show the results of the cumulative weighted rainflow cycle counting of the stress spectra for two of the eight critical points identified in Sec. IV. Figures 15a and 16a show the overall representation and Figs. 15b and 16b present the same information using a different scaling of the vertical axis to effectively zoom in on the lower cycles. Note that certain values may be clipped in the zoom-in process.

These cycles are further converted to equivalent fully reversed stress cycles at zero mean using fatigue failure criteria in order to use the experimental *S–N* curve data that are mostly available at zero stress ratio. Several fatigue failure criteria described in literature [21] can be used, such as the Soderberg method, the modified Goodman

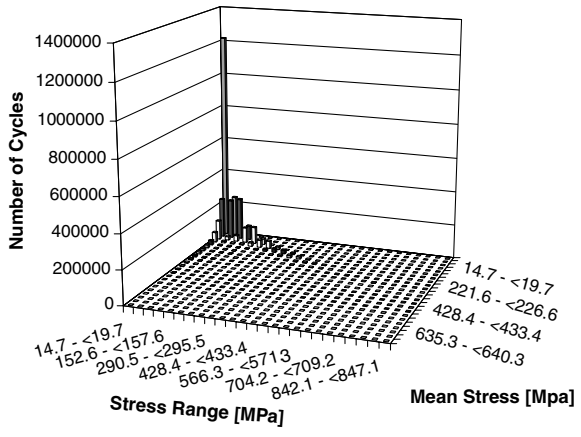

a)

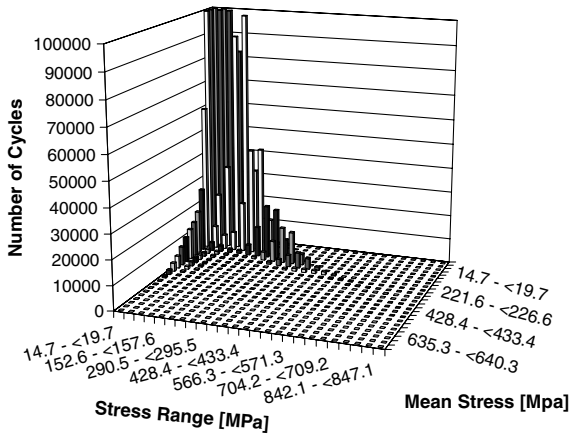

b)

Fig. 15 Rainflow cycle counting results for point 1 (per 10,000 flight hours).

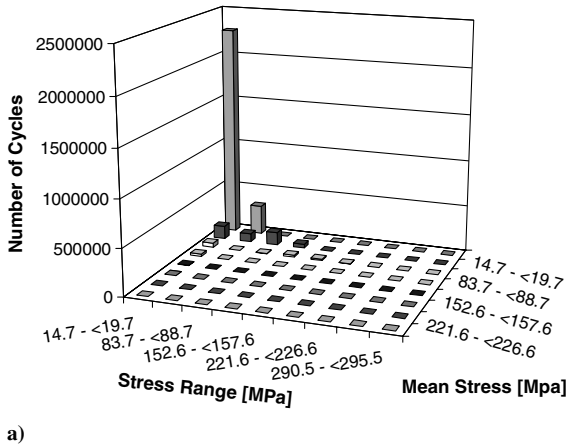

a)

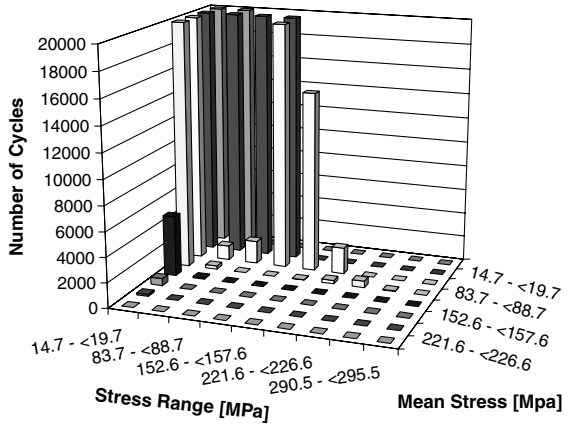

b)

Fig. 16 Rainflow cycle counting results for point 5 (per 10,000 flight hours).

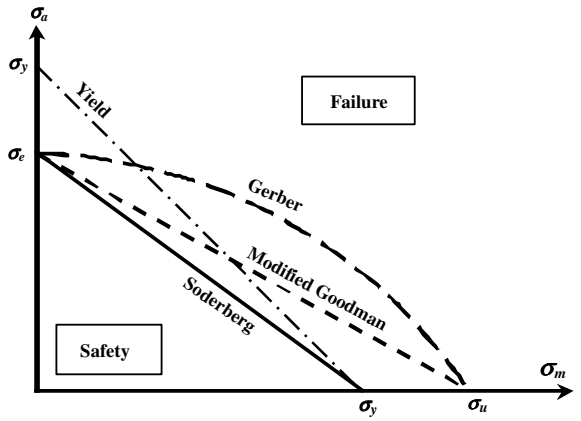

Fig. 17 Schematic of fatigue failure criterion.

method, and the Gerber method (as shown in Fig. 17). Among them, the Soderberg criterion is the only method guarding against yielding and is adopted in this analysis.

The Soderberg equation written in terms of mean and alternating stresses is

$$\frac{\sigma_a}{\sigma_e} + \frac{\sigma_m}{\sigma_y} = 1 \tag{16}$$

where σ_a and σ_m are the alternating stress and mean stress, and σ_e and σ_y are the equivalent fatigue stress at zero mean stress and yield stress of the material, respectively.

By rearranging Eq. (16), the equivalent fatigue stress at zero mean stress can be expressed in terms of the alternating mean and yield stresses as

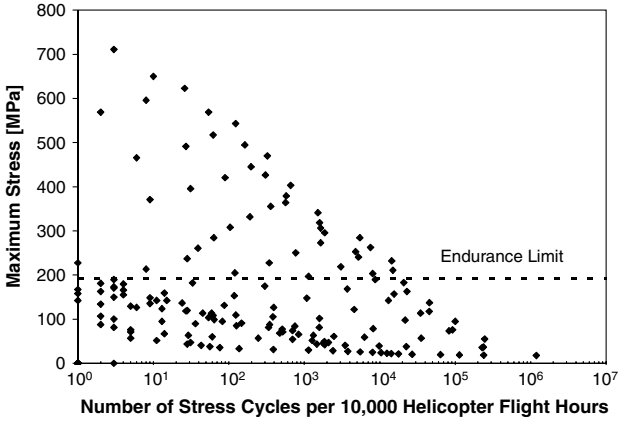

a)

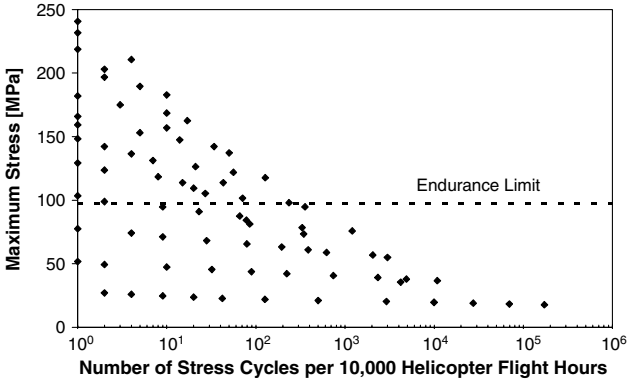

b)

Fig. 18 Shaft stress cycles at critical points a) 1 and b) 2.

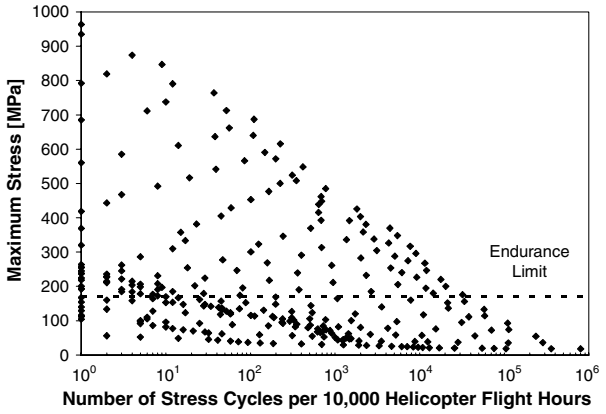

a)

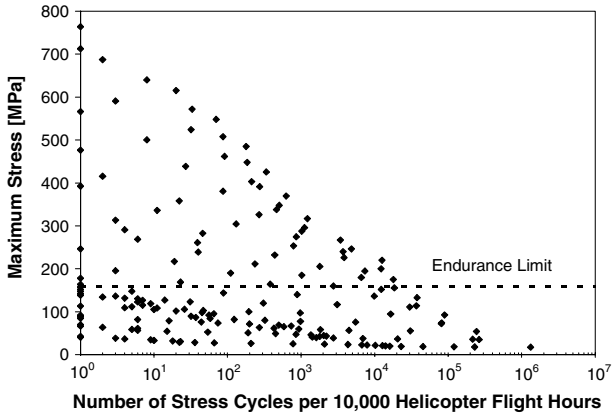

b)

Fig. 19 Inner housing stress cycles at critical points a) 3 and b) 4.

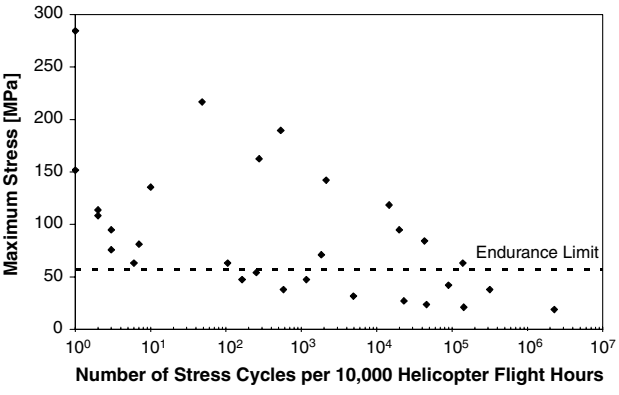

a)

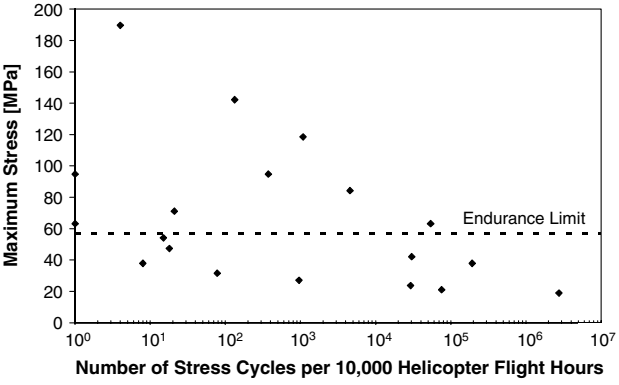

b)

Fig. 20 Outer housing stress cycles at critical points a) 5 and b) 6.

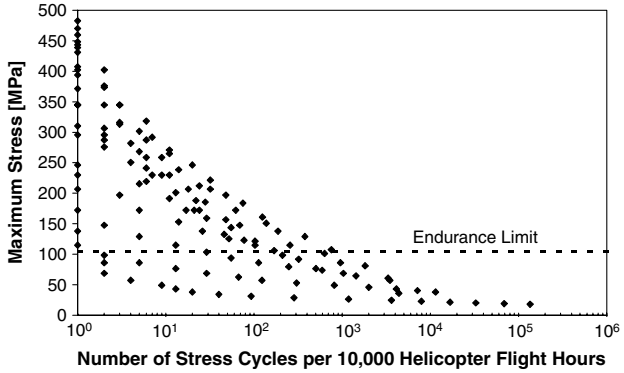

a)

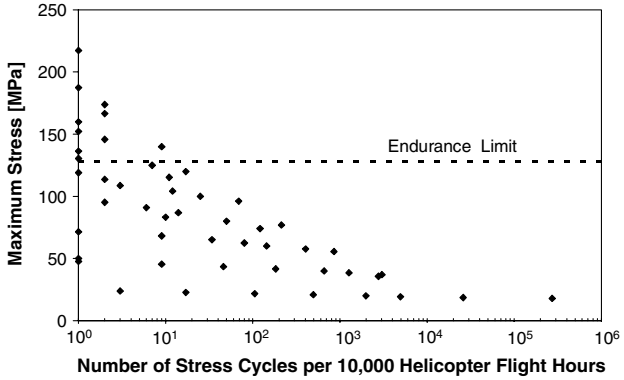

b)

Fig. 21 Spherical nut stress cycles at critical points a) 7 and b) 8.

$$\sigma_e = \frac{\sigma_a}{1 - \sigma_m/\sigma_y} \tag{17}$$

B. Estimation of Fatigue Life with Flaw Tolerance Analysis

The equivalent fatigue stresses at the critical locations are calculated by using the fatigue stress spectra and Eq. (17). The expected fatigue life of the probe components can be determined using the Palmgren–Miner cumulative damage analysis [21]. The Palmgren–Miner rule states that the cumulative total fatigue damage D_t is composed of damage contributions D_i arising from stress cycles occurring at each stress level, such that

$$D_t = \sum_{i=1}^{m} \frac{n_i}{N_i} \tag{18}$$

where m is the total number of distinct stress levels, n_i is the number of cycles expected during the design life at the distinct stress level σ_i, and N_i is the number of cycles that would cause crack initiation under the same stress level (based on the *S–N* curves of material testing).

Table 4 Cumulative damage analysis results for each critical location

Critical point	Cumulative damage per 10,000 flight hours, D_t	Calculated fatigue life in flight hours, $=10,000/D_t$	Design life in flight hours, 10,000 h
1	0.049284	>10,000	Exceeded
2	0.000443	>10,000	Exceeded
3	0.906528	11,031	Exceeded
4	0.129332	77,320	Exceeded
5	0.535223	18,683	Exceeded
6	0.047603	>10,000	Exceeded
7	0.406966	24,572	Exceeded
8	0.000325	>10,000	Exceeded

The *S–N* curves are the experimental results of smooth specimen conducted in the laboratory conditions and are not necessarily reflective of the actual components as manufactured that contain flaws [22]. As a result, these *S–N* curves need to be adjusted to yield working *S–N* curves that reflect the actual conditions of the probe components to account for various flaws as well as a life-reduction factor. The modifying factors that were taken into consideration include: surface finish condition of the parts K_f; size effect of the parts K_d; impact load factor K_l; reliability factor K_r; temperature factor K_t; and corrosion factor K_c [23–26]. Thus, the corrected fatigue endurance stress limit S_e can be expressed as

$$S_e = S_{e0} K_f K_d K_l K_r K_t K_c \tag{19}$$

where S_{e0} is the nondegraded endurance stress limit.

Once the (as manufactured) working *S–N* curves were reduced by the preceding modifying *K*–factors, an additional factor referred to as the life reduction factor was applied to fatigue cycles less than 10^4. The life reduction factor conservatively adjusts the low-cycle fatigue performance of the material. A life reduction factor of four is typically used for helicopter components [27].

Thus, the expected fatigue life of the probe assembly is given by

$$\text{fatigue life} \quad = \quad \text{design life}/D_t \tag{20}$$

where D_t is evaluated using the adjusted, working *S–N* curves to account for manufacturing flaws.

C. Fatigue Life Estimation

The stresses at each critical location calculated in the previous section occur at various stress alternates with an associated nonzero mean value. These alternating stresses with nonzero mean stresses were converted to fully reversed alternating stresses at zero mean stress using the Soderberg equation (17). The resulting stresses and corresponding cycles at each critical point were then compared against the working fatigue *S–N* curves, developed in the previous section to determine the fatigue cumulative damage using the Palmgren–Miner rule.

Figures 18–21 show the expected number of cycles, over the 10,000 flight-hour design life of the probe, at specific values of fatigue stress for each critical point in the probe (refer to Sec. IV). The endurance stress limits (dashed lines) in each figure represent the values obtained from the working *S–N* curves that have taken the flaw factors into consideration. It should be noted that the probe components are composed of different materials, hence the differing endurance limits across each figure.

A quick examination of the preceding figures shows stress cycles exceeding the endurance limit of the specific material leading to an impact on the fatigue performance of the component. However, the majority of the stresses above the endurance limit occurred at relatively low cycles. The exception to this is the inner and outer housings (Figs. 19 and 20) in which a large number of cycles at high stresses were observed. This provides an immediate indication that the resulting fatigue lives on these two components would be relatively low. The exact life is not known until a cumulative damage analysis is performed using the Palmgren–Miner rule.

The results of the cumulative damage analysis are summarized in Table 4 indicating a minimum fatigue design life of 11,031 flight hours, which exceeds the minimum 10,000 flight-hour design requirement.

VII. Conclusions

This paper develops a framework of dynamic simulation driven fatigue life analysis of a helicopter landing probe for a typical 12-ton tricycle landing gear helicopter for embarked operations on a typical frigate. The fatigue life analysis of the probe assembly consists of two subtasks: 1) the novel dynamic helicopter/ship interface simulation using Dynaface to generate the time histories of probe loads, and 2) the cumulative fatigue damage analysis of the probe assembly.

The dynamic analysis of the ship/helicopter interface generated probe loads over a wide range of operating and environmental conditions that the helicopter can be expected to operate over its service life. Each dynamic simulation was performed for an extended time period to capture, with a minimum 99.9% confidence level, all the possible probe loads, otherwise they would be practically unobtainable even by limited sea trial testing. The simulated radial and vertical probe load time histories were then converted to equivalent stresses based on the unit-load FE analysis of the individual probe structure. The critical stress locations on each probe component were identified and the time histories of the critical stress were calculated using the simulated probe load time histories. These stress time histories were then postprocessed, using the established rainflow cycle counting methodology, to determine the associated number of cycles at specific stress ranges and mean values. Weighted functions, representing the probability of occurrence of each operating condition over the 10,000 flight-hour design life were then applied to each load case to modify the rainflow cycle counts. Using the Palmgren–Miner rule and the working fatigue *S–N* curves, accounting for the manufacturing flaws, the cumulative fatigue damages over the expected 10,000 flight-hour service life were calculated. The results of the analysis indicate that the probe has a fatigue life or recommended retirement time of 11,031 flight hours, which is greater than the required design life, and was primarily dominated by the radial loading on the probe. The fatigue life calculations were based on a series of conservative assumptions. In reality, the probe will likely have a longer life. A fatigue life testing will be performed in the future to validate the dynamic simulation driven fatigue life analysis.

By integrating the novel dynamic helicopter/ship interface simulation, the rainflow cycle counting method, the FE method, and the cumulative fatigue damage analysis into one analysis environment, this new approach provides an innovative and efficient design tool by virtual prototyping that can speed up the design process and reduce the cost.

References

[1] Pro/ENGINEER Mechanica Wildfire Ver. 2.0, Parametric Technology Corp., Needham, MA, 2002.

[2] Blackwell, J., and Feik, R. A., "A Mathematical Model of the On-Deck Helicopter/Ship Dynamic Interface," Aeronautical Research Labs Rept. B870031, Melbourne, Australia, Sept. 1988.

[3] McTaggart, K. A., "SHIPMO07: An Updated Strip Theory Program for Predicting Ship Motions and Sea Loads in Waves," Defence Research Establishment Atlantic, TM 96/243, Dartmouth, NS, Canada, Mar. 1996.

[4] Shin, Y. S., Belenky, V. L., Lin, W. M., Weems, K. M., and Engle, A. H., "Nonlinear Time Domain Simulation Technology for Seakeeping and Wave-Load Analysis for Modern Ship Design," *Transactions: The Society of Naval Architects and Marine Engineers*, Vol. 111, Oct. 2003, pp. 557–583.

[5] Langlois, R. G., LaRosa, M., and Tadros, A., "Development, Validation, and Application of the Dynaface Helicopter/Ship Dynamic Interface Simulation Software Package," *Proceedings of the 2003 Summer Computer Simulation Conference*, Society for Modeling and Simulation International, San Diego, CA, 20–24 July 2003, pp. 166–176.

[6] Langlois, R. G., LaRosa, M., and Tadros, A., "Helicopter/Ship Dynamic Interface Simulation Dynaface Release 7.0," Indal Technologies, Rept.04-755, Mississauga, ON, Canada, 2004.

[7] Langlois, R. G., Zhu, Z. H., and LaRosa, M., "Analysis of Shipboard Securing and Handling of Skid-Equipped Rotorcraft," *Proceedings of the 2008 Spring Simulation Multiconference*, Ottawa, Society for Modeling and Simulation International, San Diego, CA, Apr. 2008, pp. 709–719.

[8] García de Jalón, J., and Bayo, E., *Kinematic and Dynamic Simulation of Multibody Systems*, Springer–Verlag, New York, 1994.

[9] Smiley, R. F., and Horne, W. B., "Mechanical Properties of Pneumatic Tires with Special Reference to Modern Aircraft Tires," NASA TR R-64, 1980.

[10] Zan, S. J., "A Wind Tunnel Investigation of Loads for an On-Deck Helicopter Rotor in Beam Wind," National Research Council of Canada Inst. for Aerospace Research, TR LTR-A-007, Ottawa, Apr. 1997.

[11] Zan, S. J., "Parametric Investigation of On-Deck Rotor Loads in Beam Winds," National Research Council of Canada Inst. for Aerospace Research, TR LTR-AL-2003-0064, Ottawa, Sept. 2003.

[12] "Standardized Wave and Wind Environments and Shipboard Reporting of Sea Conditions," NATO Military Agency for Standardization, STANAG 4194, Apr. 1983.

[13] "Wind and Wave Climate Atlas: The East Coast of Canada," Vol. 1, MacLaren Plansearch, TP 10820 E, Halifax, NS, Canada, Mar. 1991.

[14] Lloyd, A. R. J. M., "Seakeeping: Ship Behaviour in Rough Weather," 2nd ed., published by the author, Gosport, Hampshire, U.K., 1998.

[15] Saunders, S. (ed.), *Jane's Fighting Ships: 2002–2003*, Jane's Information Group, Alexandria, VA, 2002.

[16] Comstock, J. P., *Principles of Naval Architecture*, Society of Naval Architects and Marine Engineers, New York, 1967.

[17] Korvin-Kroukovsky, B. V., *Theory of Seakeeping*, Society of Naval Architects and Marine Engineers, New York, 1961.

[18] Fava, C., "Design Control Specification, Recover, Assist, Securing, and Traversing (RAST) System Aircraft Components,"Sikorsky Aircraft, Rept. SES-920291, Stratford, CT, Sept. 2005.

[19] "Recovery Assist, Securing and Traversing System for LAMPS MK III Helicopter," U.S. Dept. of Defense, MIL-SPEC MIL-R-85111A (AS), 1992.

[20] "Standard Practices for Cycle Counting in Fatigue Analysis," *Annual Book of ASTM Standards*, Vol. 3.01, ASTM International, Standard ASTM E1049-85, West Conshohocken, PA, 2005.

[21] Shigley, J. E., Mischke, C. R., and Budynas, R. G., *Mechanical Engineering Design*, 7th ed., McGraw–Hill, New York, 2003.

[22] "Metallic Materials Properties Development and Standardization (MMPDS)," U.S. Dept. of Transportation, Rept. DOT/FAA/AR-MMPDS-01, Jan. 2003.

[23] Bannantine, J. A., Comer, J. J., and Handrock, J. L., *Fundamentals of Metal Fatigue Analysis*, Prentice–Hall, Englewood Cliffs, NJ, 1990.

[24] Johnson, R. C., "*Machine Design*," Vol. 45, No. 11, Penton, Cleveland, OH, 1973, p. 108.

[25] Hindhede, U., Zimmerman, J. R., Hopkins, R. B., Erisman, R. J., Hull, W. C., and Lang, J. D., *Machine Design Fundamentals: A Practical Approach*, Wiley, New York, 1983.

[26] Norton, R. L., *Machine Design: An Integrated Approach*, 2nd ed., Prentice–Hall, Englewood Cliffs, NJ, 2000.

[27] Bristow, J. W., and Irving, P. E., "Safety Factors in Civil Aircraft Design Requirements," *Engineering Failure Analysis*, Vol. 14, No. 3, Apr. 2007, pp. 459–470.
doi:10.1016/j.engfailanal.2005.08.008